AFRL-AFOSR-CL-TR-2019-0002

SURFACE PLASMON RESONANCE

Joewono Widjaja
SURANAREE UNIVERSITY OF TECHNOLOGY
111 UNIVERSITY AVENUE
MUANG, NAKHON RATCHASIMA, 30000
TH

03/16/2019
Final Report

Air Force Research Laboratory
Air Force Office of Scientific Research
Southern Office of Aerospace Research and Development
U.S. Embassy Santiago, AV. Andrews Bello 2800 Santiago, Chile

REPORT DOCUMENTATION PAGE

Form Approved
OMB No. 0704-0188

1. REPORT DATE *(DD-MM-YYYY)*	2. REPORT TYPE	3. DATES COVERED *(From - To)*
16-03-2019	Final	30 Sep 2016 to 29 Sep 2018

4. TITLE AND SUBTITLE
SURFACE PLASMON RESONANCE

5a. CONTRACT NUMBER

5b. GRANT NUMBER
FA9550-16-1-0380

5c. PROGRAM ELEMENT NUMBER
61102F

6. AUTHOR(S)
Joewono Widjaja

5d. PROJECT NUMBER

5e. TASK NUMBER

5f. WORK UNIT NUMBER

7. PERFORMING ORGANIZATION NAME(S) AND ADDRESS(ES)
SURANAREE UNIVERSITY OF TECHNOLOGY
111 UNIVERSITY AVENUE
MUANG, NAKHON RATCHASIMA, 30000 TH

8. PERFORMING ORGANIZATION REPORT NUMBER

9. SPONSORING/MONITORING AGENCY NAME(S) AND ADDRESS(ES)
AFOSR/SOARD
U.S. Embassy Santiago
Av. Andres Bello 2800
Santiago, Chile

10. SPONSOR/MONITOR'S ACRONYM(S)
AFRL/AFOSR IOS

11. SPONSOR/MONITOR'S REPORT NUMBER(S)
AFRL-AFOSR-CL-TR-2019-0002

12. DISTRIBUTION/AVAILABILITY STATEMENT
A DISTRIBUTION UNLIMITED: PB Public Release

13. SUPPLEMENTARY NOTES

14. ABSTRACT
This research report describes a development of the theory for the design of divergent beam-based handheld SPR sensor, experimental verification of the validity of the developed theory and testing of optical platform of the handheld SPR device. For a given range of sample refractive indices, our analytical method allows quantitative calculations of optimum beam illumination and detection parameters for equilateral and right angle prisms of different materials. Besides finding the importance of the position of the beam incident on the prism for the sensor optimization, the proposed analytical method shows that the light detector must be inclined with respect to the prism exit surface in order to prevent elongation of the detected light pattern. The mathematical relation between the resonance angle and the size of the light detector is presented. The validity of the optimal divergent beam illumination and detection has been experimentally verified by sensing
simultaneously air - water and air - ethanol. The experimental results are in good agreement with the analytical conditions even for a large range of refractive index measurements. The errors in the RI measurements are found to be smaller than 1 %, with the sensing of air gives the smallest error, while ethanol is the highest. The increase in error stems from the lower accuracy in depth detection of the broadened SPR dip. It is also found that the divergent beam-based SPR sensor has sensitivity almost the same as that of the conventional SPR sensor based on an angular interrogation technique. Finally, it can be concluded that the efficiency of the photon energy transfer does not only depend on the polarization state of the electric field of the illuminating beam, but is also determined by the incident position of the beam on the prism entrance side and the inclination angle of a light detector.

15. SUBJECT TERMS
plasmon resonance

16. SECURITY CLASSIFICATION OF:			17. LIMITATION OF ABSTRACT	18. NUMBER OF PAGES	19a. NAME OF RESPONSIBLE PERSON
a. REPORT	b. ABSTRACT	c. THIS PAGE			ANDERSEN, GEOFFREY
Unclassified	Unclassified	Unclassified	SAR		19b. TELEPHONE NUMBER *(Include area code)* 703-615-9465

SURFACE PLASMON RESONANCE

FINAL PERFORMANCE REPORT

SPONSORING/MONITORING AGENCY: Air Force Office of Scientific Research

FEDERAL GRANT: FA9550-16-1-0380

AWARDEE: Suranaree University of Technology

111 University Avenue, Nakhon Ratchasima 30000, Thailand

CAGE CODE: SJU71 DUNS: 659454511

TITLE OF PROJECT: Surface Plasmon Resonance

PRINCIPAL INVESTIGATOR: Prof. Dr. Joewono Widjaja

PERIOD OF PERFORMANCE: 30 September 2016 – 29 September 2018 **SUBMISSION DATE:** 19 December 2018

Table of Contents

1. Introduction

This document serves as the final technical report for research completed under the project entitled "Handheld Surface Plasmon Resonance Device", funded by the United States Air Force Office of Scientific Research over the period of 30 September 2016 – 29 September 2018. Organization of this document is intended to be chronological in terms of the project funding period, beginning with early research related to the surface plasmon resonance (SPR) theory, development of the theory for the design of divergent beam-based handheld SPR sensor in order to have efficient transfer of photon energy, experimental verifications of the validity of the developed theory of divergent beam illumination and detection and testing of optical platform of the handheld SPR device.

Besides having sensitivity almost the same as that of the SPR sensor based on an angular interrogation technique, the main conclusion is that the efficiency of the photon energy transfer does not only depend on the polarization state of the electric field of the illuminating beam, but is also determined by the incident position of the beam on the prism entrance side and the inclination angle of a light detector. This final report is organized into five main tasks, including:

1. Theory of surface plasmon resonance
2. Micro-prism test chip (MPTC) technology
3. Theory for design of divergent beam illumination and detection in the SPR sensor
4. Experimental verifications of the divergent beam-based SPR sensor
5. Construction and testing of the optical platform of the handheld SPR device

2. Theory of Surface Plasmon Resonance

The proposed basic science is surface plasmon resonance (SPR). SPR is a physic phenomenon in which a light energy is converted to an energy of surface plasmon wave (SPW) [1]. Thus, when the SPR occurs, a part of incident light vanishes and the SPW is generated.

The SPR occurs only when a specific condition is satisfied, which is when the wave propagation constant of the SPW is the same as the wave propagation constant of the vanishing light wave [1]. Thus the vanishing light is transformed into the SPW. The SPW propagates at the interface of a metal layer and a dielectric medium. The propagation constant of the SPW depends on the dielectric constant of the dielectric medium, among others.

However, a propagating light wave cannot generate the SPW, because their dispersion relations (ω/k) cannot match. Therefore, a propagating light wave must be changed into a non-propagating evanescent light wave, so the dispersion relation of the SPW can match the dispersion relation of the non-propagating evanescent light wave, and the non-propagating evanescent light wave can transform into the SPW [2].

The SPW is not light or EM wave. Plasmon wave is an electron density wave. A metal may exhibit collectively longitudinal oscillations of the free electron gas density. A plasmon is a quantum of the oscillation of the free electron gas density. The SPW is a collection of plasmons that are confined to a surface [3]. It is hard to detect SPW especially its characteristics. Accordingly, instead detecting directly the SPW, one may detect the vanishing light wave. If a part of the incident light wave vanishes, it indicates that a corresponding SPW is generated.

A popular optical setup to generate the SPW is shown in Fig. 1, which is known as Kretschmann geometry or Kretschmann configuration [4,5]. A dielectric sample is placed on top

of a metal layer coated on a glass prism, such that the SPW may be generated and propagated at the interface of the metal layer and the dielectric medium.

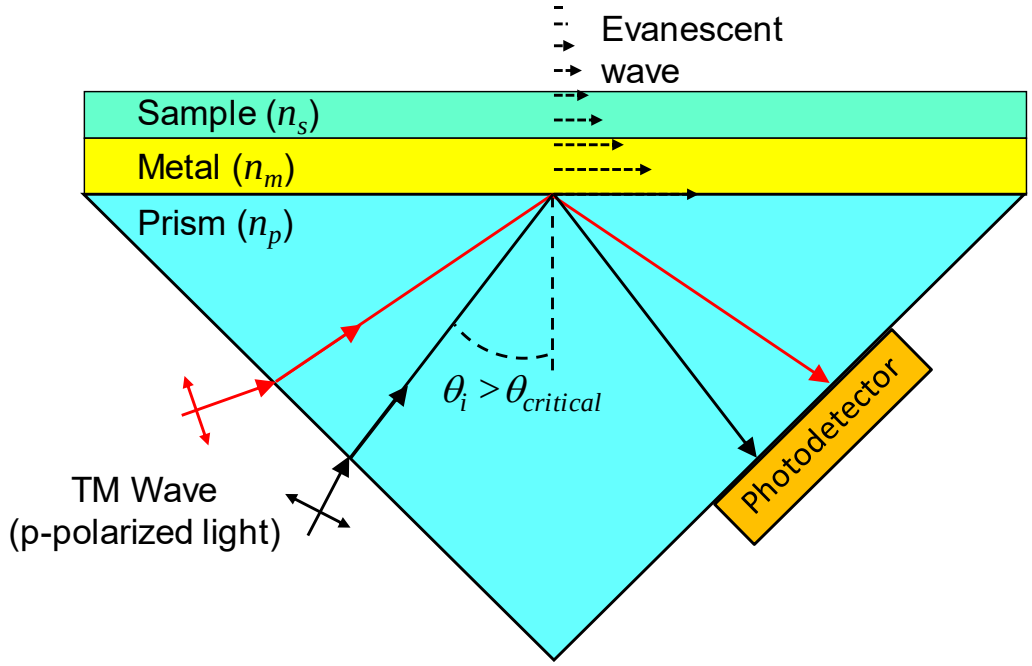

Figure 1. Kretschmann geometry for generating the SPW.

Transverse magnetic (TM) or *p*-polarized laser light is used to generate the SPW. However, since a propagating light wave cannot generate the SPW, the propagating laser light is changed into a non-propagating evanescent wave. A laser light is directed to a prism. If the incident angle θ_i at the prism-metal interface is larger than the critical angle, the incident laser light is fully reflected at the prism-metal interface due to the total internal reflection. Since the metal layer is very thin, the critical angle at the prism-metal interface is the same as the critical angle when no metal is coated on the prism.

In the total internal reflection, the incident light wave generates a non-propagating evanescent light wave at the prism-metal interface. The generated non-propagating evanescent

wave in turn generates a reflected propagating light wave at the same prism-metal interface. If the energy of the non-propagating evanescent light wave is not converted into other energy, all-energy of non-propagating evanescent light wave will be transformed back to the reflected propagating light wave, such that total internal reflection takes place.

If the energy of the non-propagating evanescent light wave is converted into the energy of the SPW, the reflected propagating light wave will not be generated – the reflected light vanishes. Thus, instead of directly detecting the SPW, one may detect the absence of the reflected propagating light wave. If the reflected propagating light wave is absent, it indicates that the SPW is generated – the non-propagating evanescent light wave is transformed into the SPW [6].

As discussed previously, the SPR occurs only when the wave propagation constant of the SPW is the same as the wave propagation constant of the non-propagating evanescent light wave. The propagation constant of the SPW depends on the dielectric constant of the dielectric medium, among others. On the other hand, the propagation constant of the non-propagating evanescent light wave depends on the incident angle of the incident propagating light wave at the prism-metal interface. In other words, if we know the incident angle of the vanishing light wave, we will know the dielectric constant of the dielectric medium.

The SPR condition can be mathematically expressed as [7]

$$k_{EW} = k_{SP}\,, \tag{1}$$

$$\left(\frac{\omega}{c}\right)\sqrt{\varepsilon_p}\,\sin\theta_r = \left(\frac{\omega}{c}\right)\sqrt{\frac{\varepsilon_m\varepsilon_d}{\varepsilon_m+\varepsilon_d}}\,, \tag{2}$$

$$\sin\theta_r = \frac{1}{\sqrt{\varepsilon_p}}\sqrt{\frac{\varepsilon_m\varepsilon_d}{\varepsilon_m+\varepsilon_d}}\,. \tag{3}$$

In the above equations, ε_p is the dielectric constant of the prism material, while θ_r is the resonance angle of incidence of the beam corresponds to the incident angle θ of the vanishing light wave. ε_m and ε_d stand for the dielectric constants of the metal and the dielectric medium, respectively. c is the speed of light and ω is the frequency of incident light.

Accordingly, one application of SPRs is to verify the presence of a dielectric material having a known dielectric constant or to find the dielectric constant of a dielectric material, because the incident angle of the vanishing light wave can be determined from observation.

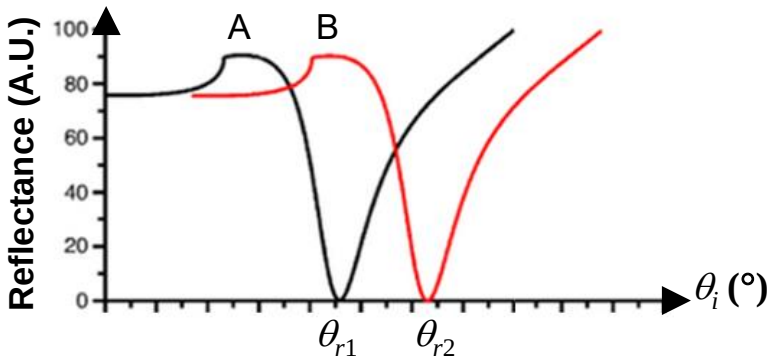

Figure 2. SPR reflectance as a function of the incident angle θ_i.

Figure 2 shows the SPR reflectance as a function of the incident angle θ_i. illustrated in Fig. 1. The SPR reflectivity A is produced by the *p*-polarized beam represented by the black line in Fig. 1, while the reflectivity B corresponds to the red beam. They have different incident angles. At the resonance condition, there is the transfer of energy from the incident beam to the SPW propagating at the interface between the dielectric medium and the thin metal layer resulting in a reduction of intensity of the reflected beam. The SPR reflectivity curve A shows a sharp dip at resonance angle θ_{r1}. The value of θ_{r1} can be determined from the curve A, which may be obtained from

measurement. If the dielectric constants of the prism and the thin metal layer are known, the dielectric constant of the dielectric medium in contact with the thin metal layer can be determined by using Eq. (3). Thus the refractive index of the dielectric medium can also be determined. Furthermore, when the refractive index of the dielectric medium changes, the reflectance dip shifts to another angle accordingly. For example, the SPR dip of the curve A shifts to the curve B, from θ_{r1}.to θ_{r2}. If the refractive index of a solution is related to the concentration of a component in the solution, the concentration of the component can be determined as well.

Therefore, in order to monitor refractive index changes, the SPR sensor must provide p-polarized beam with different angles of incidence. This is known as an angular interrogation technique which can be divided into three configurations, namely, fixing incident beam rotating prism, angle scanning (fixing prism and scanning incident beam) and fan-shaped beam [6]. The first and the second configurations are bulky since they require motorized rotation stages in order to achieve high angular resolution and sensitivity [8,9]. The other deficiency is involvement of mechanical movement which makes the system to be prone to error and low accuracy [10]. However, that problem has been solved by using fan shaped beam, which can be diverging or converging beam. The converging case requires two lenses: The first lens focuses the readout beam onto a small spot on a sensing area, while the second one collimates the reflected beam. In the diverging beam illumination, no focusing and collimating lenses are required. Due to its simplicity, implementations of SPR biosensor using the divergent beam generated from a light emitting diode, a cylindrical lens and a laser diode have been separately reported [11-13]. Recently, in order to have divergent illumination with uniform photo energy distribution and wider fan angle, use of Powell lens has been reported [14,15]. Since it provides bigger sensing area, it can be used to implement multichannel biosensors.

Figure 3 illustrates the application of a SPR biosensor to a verification of the presence of a sample or analyte [7]. SPR biosensor is a sensing device which consists of a biorecognition element (probe) on the metal layer and is able to capture a selected analyte (sample or target). The biorecognition elements (probes) are immobilized in the proximity of the surface of a metal film supporting a SPW (also known as immobilized ligand or antibody). Analyte molecules in a liquid sample in contact with the SPR sensor bind to the biorecognition elements, producing an increase in the refractive index (refractive index is a function of dielectric constant) at the sensor surface, which is optically measured by measuring the incident angle of the vanishing incident light wave. The change in the refractive index produced by the capture of analyte molecules depends on the concentration of analyte molecules captured by the biorecognition elements on the metal layer. The biorecognition element, the analyte, and the liquid sample that contains the analyte is considered the dielectric medium on the metal layer.

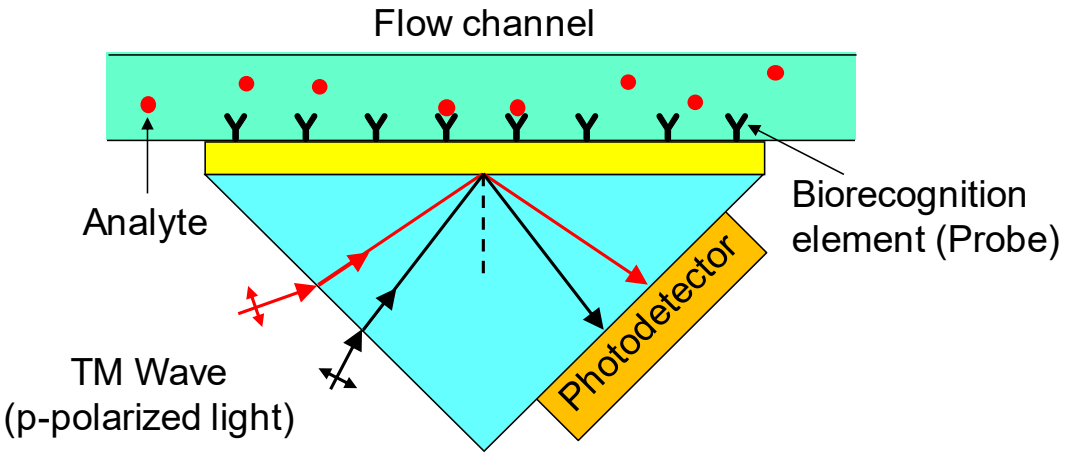

Figure 3. SPR biosensing of analyte.

In order to implement the proposed handheld SPR device, the bulky glass prism shown in Fig. 1 will be replaced with a micro-prism and the divergent beam will be used to perform the

angular interrogating measurements. Consequently, the proposed SPR device will be a compact biosensor able to measure multi analytes. Therefore, the challenge is to prove that the basic science presented above is valid for the proposed handheld SPR device. Since we do not or cannot directly detect the SPW, we detect the vanishing incident light wave. Thus, we want to verify first, whether the energy of the incident light wave that satisfies the SPR condition can be efficiently converted to the energy of the SPW for given large sensing area and second, what is the sensor sensitivity.

If the conversion efficiency is low, it is hard to detect the vanishing incident light wave. If the conversion efficiency is high, it would be easy to detect the vanishing incident light wave. In other words, if the conversion efficiency is high, the signal-to-noise ratio of the measurement will be accordingly high. If the conversion efficiency is low, we will analyze theoretically and investigate experimentally how to improve the conversion efficiency. This is a crucial issue, but up to now, very few studies are conducted.

The proposed research will lead to a vital science breakthrough which is a high conversion efficiency of the incident light wave to the SPW. A high conversion efficiency of the incident light wave to the SPW is the key and fundamental issue for the success of all kinds of SPR biosensors, not limited to the proposed system.

3. Micro-Prism Test Chip (MPTC)

As mentioned in the previous section, the proposed system will be implemented by replacing the bulky glass prism of Fig. 1 with a micro-prism, which is fabricated by a special technique similar to a glass fiber drawing technique [16]. The micro-prism serves as a part of a disposable test chip. In the conventional approach, the disposable test chip and prism are two separate components, the bulk prism is built in to the equipment and the disposable test chip is usually a piece of glass slide

with processed bio-specific element on the top surface. The disposable test chip, e.g., glass slide, is attached to the bulk prism with index matching fluid and will be discarded after a single or multiple uses. In the proposed system, there is no disposable glass slide. The micro-prism is disposable. Since no glass slide test chip is required, the need of using index matching fluid will be eliminated and the switching between tests will be easy.

The fabrication method for micro-prism is similar to the glass fiber drawing technique. Due to the nature of this glass drawing technique, because it includes cross-sectional size reduction and fire polish, the drawn micro-prism exhibits very high quality surface finish without any subsequent grinding and polishing. Thus the cost may be tremendously low.

There are three major advantages of drawing micro-prism: (1) no initial or subsequent mold cost is required, (2) the precision and product uniformity is excellent, and (3) the combination geometry reduction and fire polishing nature of this process produces very high quality diffraction limited surface finish that may improve the quality of SPR measurement result.

The process involves a drawing tower similar to that for optical fiber production as shown in Fig. 4(a). The drawing process is relatively straightforward. A glass preform having a shape of prism is suspended vertically above a furnace or oven and lowered slowly. Once inside the heat zone, the lowest part of the glass preform softens and is pulled from below at a rate exceeding that of the feed into the furnace depending on the desired cross-sectional size reduction. The proper pull rate can be calculated based on the feed rate and the conservation of mass in and mass out. The furnace may be temperature controlled. The size of the micro-prism pulled from the furnace may be in-situ close loop controlled by a laser micrometer during the pulling. The drawn micro-prism can be segmented to an appropriate length.

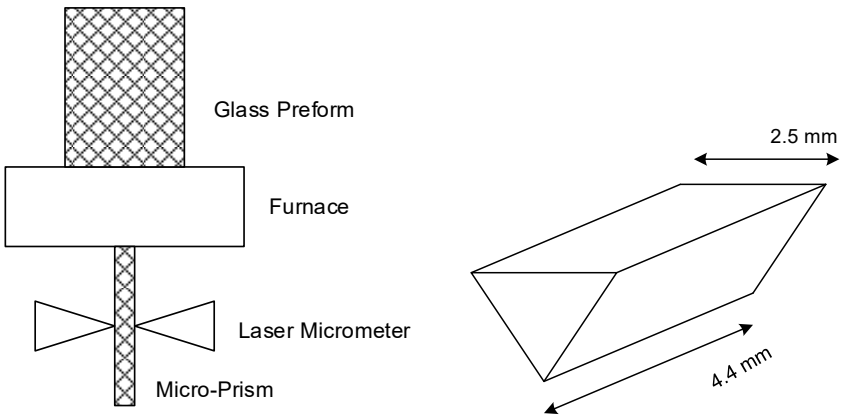

(a) (b)

Figure 4. (a) Drawing process of a micro prism and (b) geometry.

of the fabricated micro prism.

Figure 4(b) shows an exemplary geometry of a fabricated equilateral triangular micro-prism. Each side of the drawn micro-prism may be approximately 2.5 mm. The length of the segmented micro-prism may be approximately 4.4 mm for a test chip. One side surface of the micro prism is coated with a thin metal layer, for example, the metal may be gold, silver, aluminum, copper, or other suitable metals.

4. Design of Divergent Beam Illumination and Detection in SPR Sensor

Instead of directly testing the fabricated micro-prism, we will test the proposed optical system using a larger size prism (about 10 times of the size of the micro prism). After testing and confirming the performance of the optical system, we will replace the larger size with the micro-prism. The larger size prism is identical to the micro-prism, except the size is larger. The divergent illumination with uniform beam profile and wide fan angle is generated by using Powell lens.

Although the SPR sensor using Powell lens has been proposed, the reported works did not address several optical aspects which are important for optimizing the sensor performance [14,15].

In the following, optical aspects for performance optimization of the handheld SPR sensor are studied. The first aspect is the determination of the fan and the illumination angles of the divergent beam for a given refractive index to be measured. The second one concerns with the position of an array light detector with respect to the reflected output beam. The third one is the mathematical relation between the spatial position along the sensor plane and the resonance angle. The final one is the dependency of the sensing parameters on the prism types and materials.

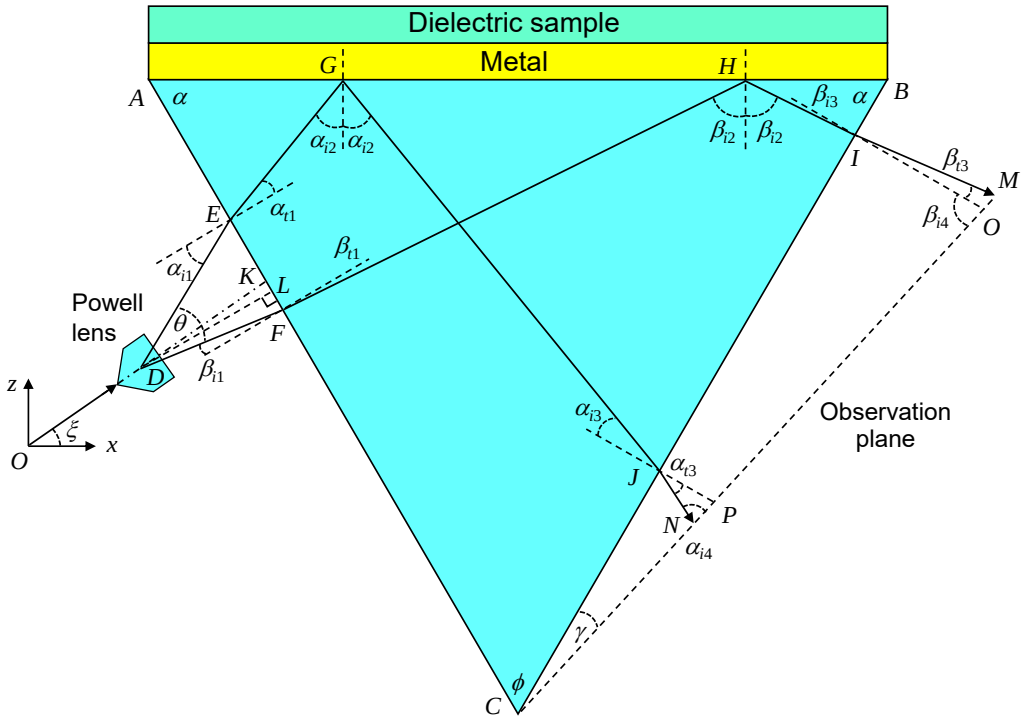

Figure 5. Schematic diagram of Kretschmann-based SPR sensor using the divergent beam illumination.

In order to understand the above aspects, the present study is conducted by using bulky equilateral (EQ) and right angle (RA) prisms with different materials. A gold coated glass is placed on top the prism having index matching liquid between the glass and the prism. For the sake of experimental simplicity, we use a HeNe laser emits visible light. The *p*-polarized beam is generated by transmitting this laser light through a polarizing beamsplitter cube shown in Fig. 5. The polarization state of the laser beam is controlled by a half wave plate such that a rotation of the half wave plate by ϕ around the beam axis results in 2ϕ rotation of the beam polarization state. This will be used to maximize the transfer of photon energy. After passing Powell lens with a fan angle θ, the uniformly spreading p-polarized beam is obliquely incident on the prism side *AC* so that the refracted beam strikes the interface between the prism – gold coated glass at an angle larger than the critical angle. Besides causing evanescent waves penetration in the normal direction through the film, the reflected beam confined by the rays *GJ* and *HI* impinges on the prism side *BC*. One particular light ray reflected at the angle at which the surface plasmon resonance occurs has the lowest photon energy. The vanishing light can be detected by means of an array light detector placed on an inclined observation plane. The inclination of the observation plane is to ensure that the reflected beams *IM* and *JN* will have the same value of the angles of incidence on the light detector. Consequently, the resonance angle can be detected, yielding the refractive index of the sample being analyzed.

4.1 Fan and Illumination Angles

To implement the SPR sensor using the divergent light illumination, it is assumed that the refractive index of sample to be measured has a resonance angle within the incident angles α_{i2} and β_{i2} of the rays *EG* and *FH*, respectively. As a consequence, this divergent read out beam has the

range of measurable angle $\Delta\theta = \beta_{i2} - \alpha_{i2}$. After determining the angle α_{i2}, the angle of incidence α_{i1} at the surfaces *AC* can be derived by using the Snell's law, resulting in

$$\alpha_{i1} = \arcsin[n_p \cos(\phi/2 + \alpha_{i2})], \tag{4}$$

with ϕ represents the prism apex angle. In similar fashion, the angle of incidence β_{i1} can also be obtained by using the angle β_{i2}. As a result, the fan angle of the readout beam can be mathematically expressed as

$$\begin{aligned}\theta &= \alpha_{i1} - \beta_{i1} \\ &= \arcsin\left[n_p \cos(\phi/2 + \alpha_{i2})\right] + \arcsin\left[n_p \cos(\phi/2 + \beta_{i2})\right].\end{aligned} \tag{5}$$

The above equation shows that the full beam divergence angle θ must be determined by taking into account the range of measurable angles corresponding to the refractive index to be measured and the prism material together with its apex angle. When the fan angle is determined, the illumination angle ξ can be simply calculated by using the triangle ΔOKC. It is found that the principal axis should be tilted with respect to the *x* axis by

$$\begin{aligned}\xi &= (\phi + \theta)/2 - \beta_{i1} \\ &= (\phi + \theta)/2 + \arcsin\left[n_p \cos(\phi/2 + \beta_{i2})\right].\end{aligned} \tag{6}$$

4.2 Inclination Angle of the Observation Plane

According to the geometry of light propagations, the beams *JN* and *IM* emerge from the prism at different angles that are $\alpha_{t3} = \alpha_{i1}$ and $\beta_{t3} = \beta_{i1}$, respectively. Placing a light detector parallel along the prism side *BC* will cause asymmetric light detection. Elongation of the detected light pattern may broaden the width of the dip light intensity, yielding a wrong measurement of the resonance angle. In order to solve the light distribution problem, the observation plane is inclined by using

the vertex *B* as a center with respect to the surface *BC* of the prism, yielding $\alpha_{i4} = \beta_{i4}$. The inclination angle of the observation plane can be written as

$$\gamma = (\alpha_{i1} + \beta_{i1})/2. \tag{7}$$

4.3 Beam Widths

The beam widths of *EF*, *GH* and *IJ* can be derived by using geometrical optics analysis. From three triangles Δ*DEF*, Δ*DEL* and Δ*DLF*, the beam width *EF* is dependent upon the fan angle

$$EF = \frac{DL \sin\theta}{\cos\alpha_{i1} \cos\beta_{i1}} \tag{8}$$

with *DL* is the normal distance from the prism surface *AC* to the focal point of the lens.

The beam width *GH* can be mathematically derived from triangles Δ*AGE* and Δ*AHF*. Subtractions of

$$AG = \frac{AE \sin(\phi/2 + \alpha_{i2})}{\cos\alpha_{i2}} \tag{9}$$

from *AH*

$$AH = \frac{(AE + EF)\sin(\phi/2 + \beta_{i2})}{\cos\beta_{i2}} \tag{10}$$

gives the beam size *GH* as

$$GH = AE\left[\frac{\sin(\phi/2 + \beta_{i2})}{\cos\beta_{i2}} - \frac{\sin(\phi/2 + \alpha_{i2})}{\cos\alpha_{i2}}\right] + EF\frac{\sin(\phi/2 + \beta_{i2})}{\cos\beta_{i2}}. \tag{11}$$

Equation (11) shows that firstly, the beam width *GH* depends highly on the range of the measurable resonance angle and the prism apex angle. Secondly, they are also dependent upon the width of the divergent beam and its incidence position *AE* measured from the vertex *A*. This equation is useful for determining the dimension of the thin gold film.

By applying the sine rule to the triangles ΔHBI and ΔGBJ, the beam positions BI and BJ can be mathematically expressed as

$$BI = \frac{(AB - AH)\cos\beta_{i2}}{\cos\beta_{i3}} \tag{12}$$

and

$$BJ = \frac{(AB - AG)\cos\alpha_{i2}}{\cos\alpha_{i3}} \tag{13}$$

respectively. Next, the beam width IJ is obtained by subtracting the beam positions BI from BJ

$$IJ = AB\left[\frac{\cos\alpha_{i2}}{\sin(\phi/2+\alpha_{i2})} - \frac{\cos\beta_{i2}}{\sin(\phi/2+\beta_{i2})}\right] - AE\left\{1 - \frac{\sin(\phi/2+\alpha_{i2})\cos\beta_{i2}}{\sin(\phi/2+\beta_{i2})\cos\alpha_{i2}}\right\}$$

$$+ GH\frac{\cos\beta_{i2}}{\sin(\phi/2+\beta_{i2})}. \tag{14}$$

It can be understood that besides the distance AE, the beam width IJ on the surface BC is governed by the size of hypotenuse AB and the beam width GH.

Owing to dependency of the beam sizes GH and IJ on the distance AE, it is important to study effects of the distance AE on the incidence positions of the rays GJ and HI on the prism side BC that are the distances JC and BI, respectively. From the polygon $EGHF$, this distance JC can be expressed as

$$JC = \frac{(AB - AE)\sin\left\{2\alpha_{i2} - \arctan\left[\frac{EC\sin(\phi/2+\alpha_{i2})\cos\alpha_{i2}}{AE\cos\phi/2 + EC\cos(\phi/2+\alpha_{i2})\cos\alpha_{i2}}\right]\right\}}{\sin\left\{\arctan\left[\frac{EC\sin(\phi/2+\alpha_{i2})\cos\alpha_{i2}}{AE\cos\phi/2 + EC\cos(\phi/2+\alpha_{i2})\cos\alpha_{i2}}\right]\right\}}. \tag{15}$$

The value of EC equals to

$$EC = AC - AE = AB - AE \tag{16}$$

for the EQ prism, while for the RA prism it is

$$EC = AC - AE = AB/\sqrt{2} - AE\,. \tag{17}$$

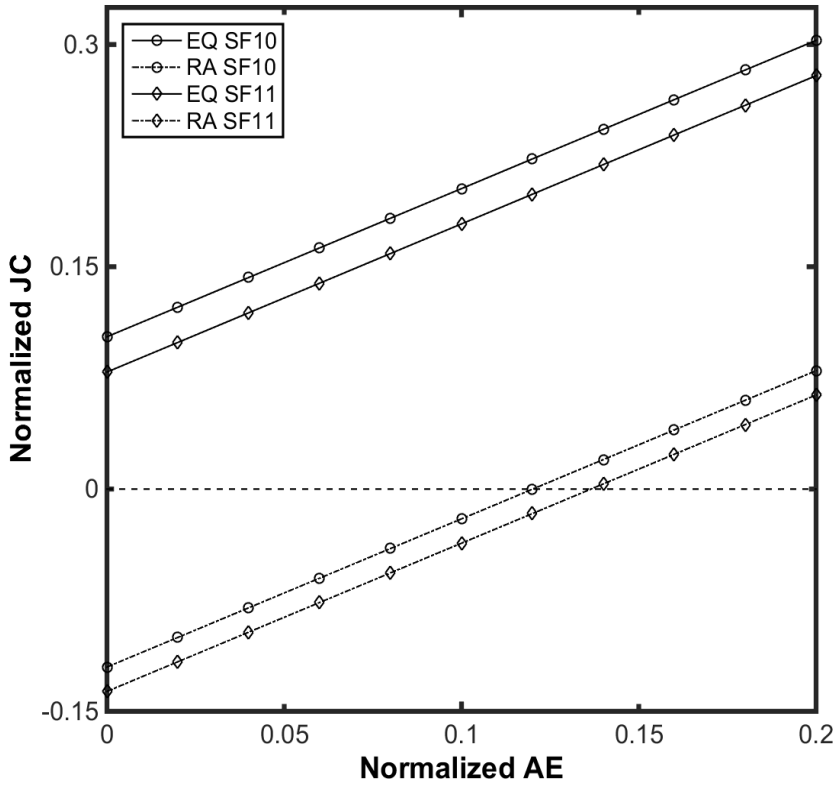

Figure 6. Dependence of the distance *JC* on the beam position *AE* for the EQ and the RA prisms of different materials.

Figure 6 shows the effects of *AE* on the distance *JC* calculated by using Eq. (15) for the EQ and the RA prisms. Their values are normalized by the side length *AB*. The solid lines with circle and diamond markers represent the normalized distances for the SF10 and the SF11 EQ prisms, respectively. The dash-dotted lines correspond to the RA prisms. It is apparent that the value of *JC* for the right angle prism varies from negative to positive as the distance *AE* increases. The negative *JC* indicates that the ray *GJ* is not incident on the surface *BC*. This can be explained by considering the argument of arctan in the numerator of Eq. (15). For *AE* = 0, this argument reduces to a ratio of $\sin(\phi/2+\alpha_{i2})$ to $\cos(\phi/2+\alpha_{i2})$. For the RA prism, the summation $\phi/2+\alpha_{i2}$ is

larger than that for the EQ prism. The sine of this large angle is nearly unity, however, its cosine is very small. Consequently, the arctan of this very high ratio value gives a resultant angle which is greater than the angle $2\alpha_{i2}$, resulting in a negative angle difference. The EQ prism does not exhibit this tendency, because its apex angle is larger. When the distance *AE* becomes longer, a decrease in the ratio results in smaller angle returned by the arctan. Furthermore, it is found that due to having higher critical angle, the prism with lower refractive index has higher value of *JC*.

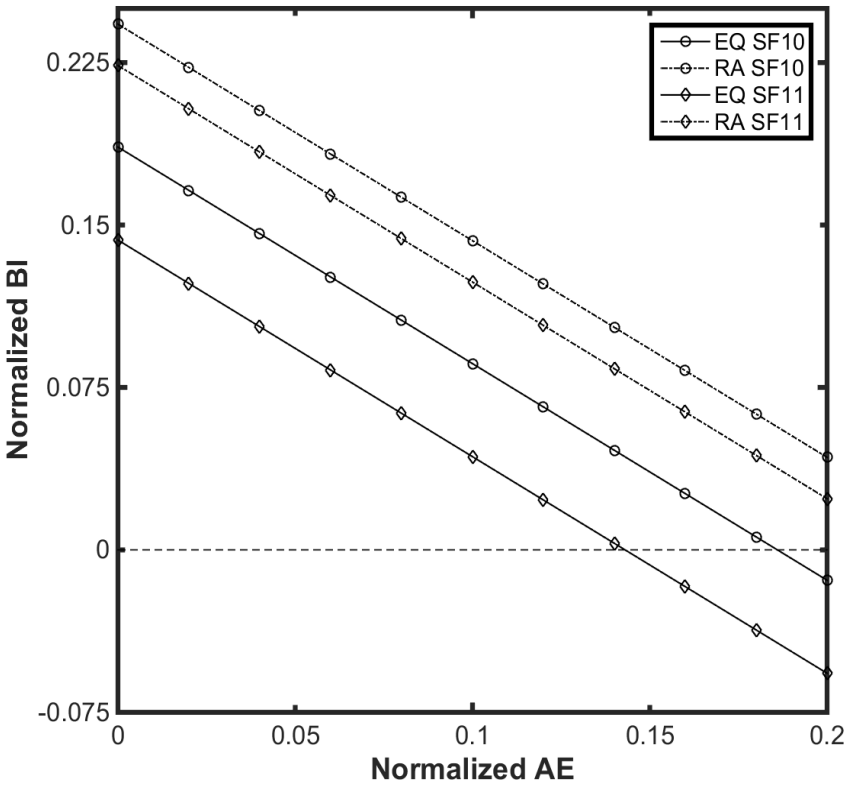

Figure 7. Dependence of the distance *BI* on the beam position *AE* for the EQ an d the RA prisms of different materials.

The effect of *AE* on the distance *BI* can be mathematically derived by substituting Eq. (10) into Eq. (12)

$$BI = \frac{AB\cos\beta_{i2} - (AE + EF)\sin(\phi/2 + \beta_{i2})}{\cos\beta_{i3}}. \quad (18)$$

Equation (18) reveals similar dependency of the distance *BI* on the position *AE*, which is plotted in Fig. 3. It is clear from Fig. 7 that the normalized distance *BI* varies with negative slope, regardless of the prism types. According to Eq. (18), the increase of the distance *AE* reduces the value of *BI*. The distance *BI* is also affected by the prism material through the beam size *EF*. This is because the prism with low refractive index requires smaller incident angles $\alpha_{i1}$and β_{i1}. For smaller *EF*, the distance *BI* becomes larger. The negative value of *BI* represents the situation that the ray *HI* does not exist. Therefore, two important conclusions can be drawn from this analysis. The first conclusion is that the beam position *AE* is determined by considering that the two distances *JC* and *BI* must be positive. The second one is that the beam illumination and detection for the RA prism is affected more severe by the position *AE* than those for the EQ prism.

Finally, the detected beam size can be obtained by calculating *MN* = *BN* – *BM*, which is derived from the triangles Δ*BIM* and Δ*BJN*. The beam size on the light detector is equal to

$$MN = \frac{IJ\cos\beta_{i1} + BI(\cos\alpha_{i1} - \cos\beta_{i1})}{\cos\gamma}. \quad (19)$$

Equation (19) can be viewed as a mapping of the resonance angle on the detecting element of the light detector. This is because the angles of incidence α_{i1} and β_{i1} are in fact determined by the range of the measurable resonance angles. It is also clear that the output beam size is proportional to the inclination angle of the light detector.

4.4 Discussions

As discussed in the preceding section, the analytical calculations show that the position of the incidence beam in the prisms is very important for optimizing the beam illumination and detection. In this section, the proposed design method is used to calculate the optimized sensor parameters.

Let us consider the measurement of the refractive index of water (n_s = 1.3317) [17] by using the two types of prism. The resonance angles of water calculated by using Eq. (3) gave β_{spr} = 54.10° and 56.80° for the SF11 (n_p = 1.785) and the SF10 (n_p = 1.728) prisms, respectively. When the sensor had the range of measurable angle $\Delta\theta$ = 23.00° and the incident angle α_{i2} was set to be equal to the critical angle of the prism, the incident angle β_{i2} could be determined. After calculating the angles of incidence α_{i1} and β_{i1}, the other angles θ, ξ and γ, were obtained by using Eqs. (5), (6) and (7), respectively. The calculated angles of the SPR sensor summarized in Table 1 reveals that the EQ prism with lower refractive index requires smaller fan and inclination angles, however, a larger illumination angle.

Table 1. Calculated angles for the SPR sensor using the EQ prism with different materials.

Refractive index	Angles							
	β_{spr} (°)	α_{i2} (°)	β_{i2} (°)	α_{i1} (°)	β_{i1} (°)	θ (°)	ξ (°)	γ (°)
1.785	54.10	34.07	57.07	51.30	5.23	46.06	47.79	28.75
1.728	56.80	35.35	58.35	46.11	2.85	44.25	49.27	24.48

Table 2. Calculated angles for the SPR sensors using the RA prism with different materials.

	Angles							
Refractive index	β_{spr} (°)	α_{i2} (°)	β_{i2} (°)	α_{i1} (°)	β_{i1} (°)	θ (°)	ξ (°)	γ (°)
1.785	54.10	34.07	57.07	19.78	-21.91	41.69	43.93	-1.065
1.728	56.80	35.35	58.35	16.84	-23.51	40.35	41.67	-3.335

In the case of the RA prisms, the calculated angles presented in Table 2 show that the fan, the illumination and the inclination angles are generally smaller than those of the EQ prisms. This shows that the important roles of the materials and the prism apex angle in the sensor optimization. Comparison between the two tables also reveals that for the RA prisms, the changes of the angle of incidence, α_{i1} and β_{i1}, caused by the refractive index are smaller than those for the EQ prisms. Therefore, the effects of the refractive index on the beam parameters in the RA prisms is less than in the EQ ones.

In order to have better insight into the beam sizes, Eqs. (8), (11), (14) and (19) were calculated by the corresponding angles presented in Tables 1 and 2. The calculations took into account the Powell lens distance DK = 0.8 cm and the prism side length AB = 5 cm. The distance AE = 0.710 cm was selected to satisfy the required positive values of JC and BI for all prism types.

Table 3. Width of the SPR beams for the EQ and the RA prisms of different materials.

Refractive index	EQ Prisms				RA Prisms			
	EF (cm)	*GH* (cm)	*IJ* (cm)	*MN* (cm)	*EF* (cm)	*GH* (cm)	*IJ* (cm)	*MN* (cm)
1.785	0.9254	2.233	2.809	3.641	0.6095	1.532	2.048	2.083
1.728	0.7917	2.069	2.654	3.325	0.5901	1.552	2.030	2.130

Table 3 presents the calculated beam sizes for both types of the prism. It is clear that in the case of the EQ prisms, higher refractive index requires larger fan angle, therefore the beam widths are generally longer. In comparison with the RA prisms, the EQ prism has longer beam size because the bigger dimension of the EQ prism causes longer beam propagation. This implies that the EQ

prism requires bigger dimension of the sensing and the light detecting areas. Owing to the insignificant difference of the angles of incidence of the RA prisms, the higher refractive index does not cause bigger beam size. Finally, the bigger inclination angle of the lower refractive index of the RA prism the results in the longer beam width *MN*.

4.5 Conclusions

Table 4. Dependency of the sensor parameters on the prism apex angle and the materials.

Sensor parameters	EQ Prisms		RA Prisms	
	High RI	Low RI	High RI	Low RI
Fan angle θ	Big	Small	Smaller	Smallest
Illumination angle ξ	Big	Small	Smaller	Smallest
Inclination angle γ	Big	Small	Smallest	Smaller
Beam widths *GH* and *MN*	Long	Short	Shortest	Shorter
Sensing and detecting areas	Big	Small	Smallest	Smaller

In order to implement the handheld SPR device, we have studied theoretically optimal divergent beam illumination and detection of the Kretchsmann-based SPR sensors by means of geometrical optics analysis. Besides finding the importance of the incident position of the illuminating beam on the prism for the sensor optimization, our analytical method shows that the light detector must be inclined with respect to the prism exit surface in order to prevent elongation of the detected light pattern. The relation between the resonance angle on the sensing area and the size of the light detector has also been mathematically established. The dependency of the sensor parameters on the prism apex angle and the materials summarized in Table 4 is useful for implementing the SPR sensor using the divergent beam illumination. For example, the smallest inclination angle and the

shortest beam widths of the RA prism with high refractive index may be useful for implementing low-cost and compact SPR sensor.

5. Experimental Verifications of the Divergent Beam-Based SPR Sensor

To verify the validity of the characteristics of the beam illumination and detection analyzed in the preceding section, the Powell lens-based SPR sensor was experimentally implemented at room temperature by using the optical setup shown in Fig. 8 with 50 mm SF11 EQ prism. The other beam parameters had the same specifications as in the above computations.

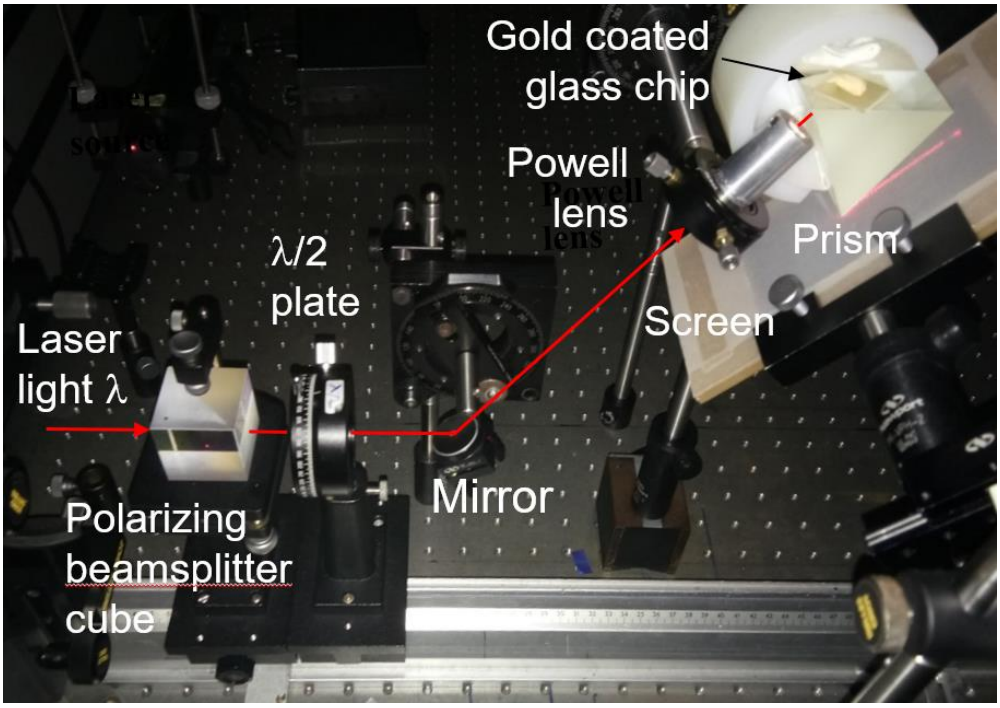

Figure 8. Experimental setup for implementing the SPR sensor using the divergent beam.

Besides water and absolute ethanol, air, which provides well-SPR characteristics, was used as test samples for calibration. For this reason, the incident angles at the sensing area had to cover the resonance angles of the three test samples from 34° to 57°. A *p*-polarized light was generated

from a He-Ne laser with an operating wavelength λ = 632.8 nm via a combination of the polarizing beamsplitter cube and the half wave plate. Powell lens having a fan angle θ = 60° produced uniformly divergent light. Each SPR measurement was conducted by attaching a 20 mm × 20 mm Au evaporated glass plates (Nano SPR, BA1000) with the refractive index n_g = 0.1726+j3.4218 [18,19] to the hypotenuse *AB*. To cover a broad range of the incident angles, the diagonal of the plate was oriented to be parallel to the prism hypotenuse. Index matching liquid (Cargille series A) was added in the gap between the prism and the glass plate in order to reduce light loss. Test liquids were drop at a particular position on the glass plate by using a 10-microlitter pipette (Glassco). The position was determined by substituting the resonance angle of the corresponding liquid into Eq. (7). Totally reflected intensity patterns were captured by using a 2D CMOS image sensor (Sony Exmor R) with 7952 × 5304 pixels in an area of 35.9 mm × 23.8 mm. In Fig. 8, instead of the sensor, a screen was installed along the *MN* direction of the observation plane. This is to confirm that the light output reflected from all incident angles at the sensing area formed a straight line pattern. As a result, unlike the conventional scanning method, the SPR reflectivity from a broad range of angles can be detected by one-shot recording.

5.1. Results and Discussions

The first experimental verification was done by measuring the SPR of water. Figure 9(a) shows the SPR reflectivity pattern captured by the CMOS sensor placed at the observation plane. According to Eq. (19), the sensor pixel along the direction *MN* corresponds to the angle of incidence β_{i2} on the sensing area. The reflected light beam occupies horizontally the whole length of the CMOS sensor. Its width in the vertical direction is about 200 pixels or about 1 mm. Two straight dark lines separate clearly the reflected pattern into three parts. They are caused by photon absorptions occurred during the resonance of surface plasmons at the gold - air and the gold - water

interfaces. The broad divergent beam ensured that two SPRs can occur simultaneously. The dark line appears on the left side of the pattern has a narrower width than the one on the right side. This is because the refractive index of air is smaller than water, the transfer of photon energy occurs over a narrower range of the angle of incidence β_{i2}, sharpening the dark SPR line. The well-defined lines indicate that the gold-evaporated glass plate used in this experiment was not contaminated.

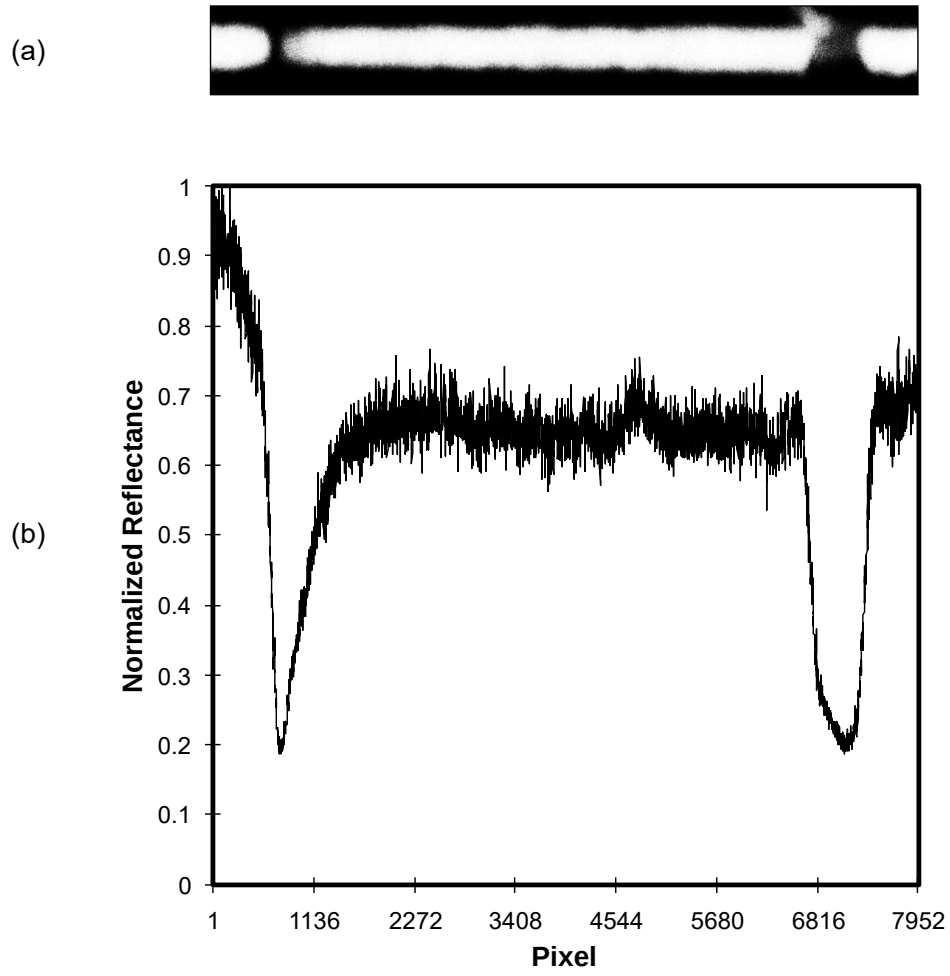

Figure 9. (a) SPR reflectivity pattern of air and water and (b) its corresponding normalized reflectivity averaged along the vertical direction.

To extract the positions of the SPR reflectivity minima, 1D intensity profile shown in Fig. 9(b) was produced by averaging the reflectivity pattern along its vertical width. Although the 1D SPR reflectivity has small intensity fluctuations, which may be caused by light scattering and non-uniform distribution of the index matching liquid, the two dip intensities can be clearly identified. The SPR dips having the lowest depth of about 0.18 was confirmed by adjusting the angle of the half-wave plate around the beam axis. It can be estimated that the energy transfer for air and water are about 73 %. This represents the best efficiency of the energy transfer from the evanescent wave to surface plasmons obtained in this work. The lowest depth position of the SPR absorption of air is detected at the pixel number 713 of the sensor, while that of the resonance of water sample is at the pixel 7107. The higher number of pixel position corresponds to the higher resonance angle.

The second experimental verification measured the SPR of absolute ethanol (n_S = 1.3580) [20]. The reflected SPR pattern and its corresponding averaged intensity are shown in Figs.10 (a) and (b), respectively. While the first dark SPR line was the same as that of the resonance of surface plasmon at the gold - air interface, the second dark line was produced by that of the gold – ethanol interfaces. In comparison with Fig. 9, the lowest depth of the reflectivity caused by the SPR absorptions of air appears at the same position. It is apparent from Fig. 10 that the SPR dip of ethanol is shifted toward to the pixel 7523 and its width is broadened. This result is consistent with the fact that the higher refractive index of ethanol caused the energy transfer from the evanescent wave to surface plasmons occurs over a broader range of the incident angle at the sensing area. The efficiencies of the energy transfer are slightly lower than the previous measurements.

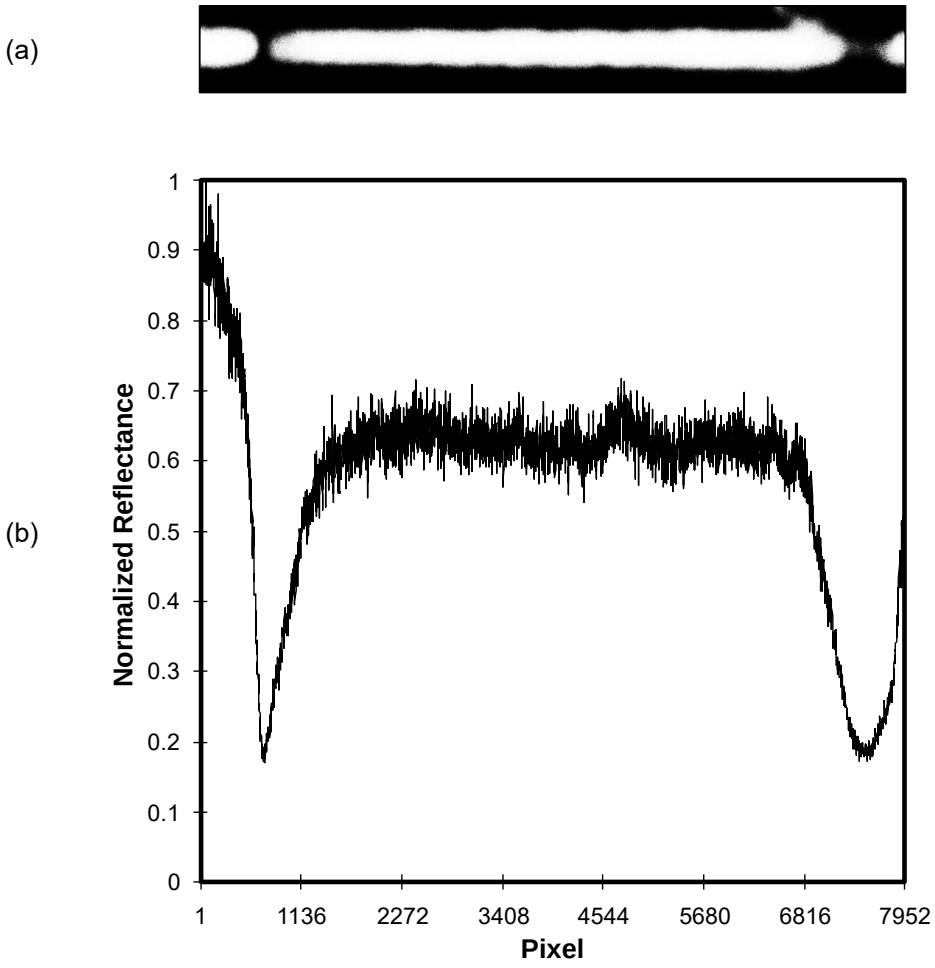

Figure 10. (a) SPR reflectivity pattern of air and ethanol and (b) its normalized reflectance averaged along the vertical direction.

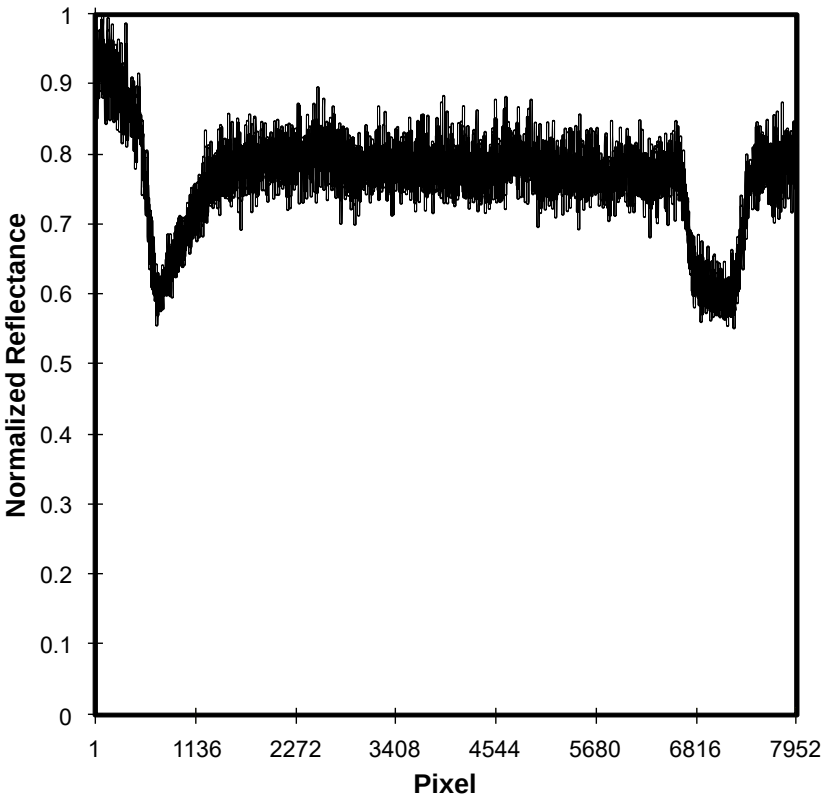

Figure 11. Normalized SPR reflectivity of air - water obtained by using partially *p*-polarized light.

Figures 11 and 12 show the normalized SPR reflectivities of air - water and air – ethanol obtained by using partially *p*-polarized light. The light was generated by means of rotating the half-wave plate 22.5° around the beam axis, yielding both *p*- and *s*- electric components. Although the transfer of the photon energy of the *p*-polarized beam into the surface plasmon wave caused the vanishing of light, the *s*-polarized beam reflected totally at the same resonance angle superposed in the same position of the SPR dip. As a result, the SPR dip intensities become higher. In comparison with the SPR reflectivities shown in Figs. (9) and (10), the current reflectivity is the result of inefficient energy transfer.

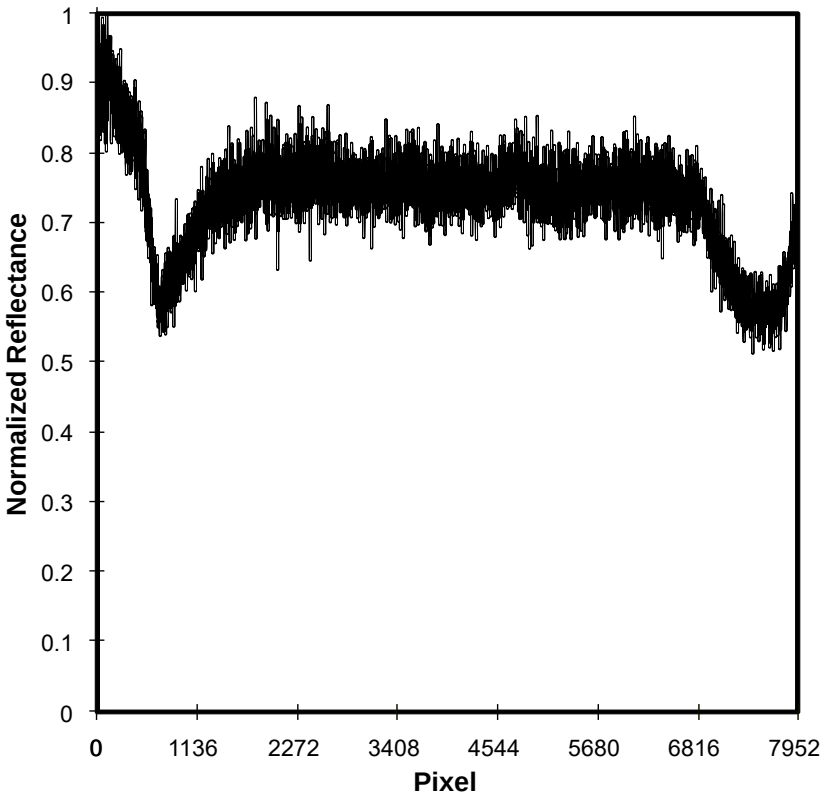

Figure 12. Normalized SPR reflectivity of air - ethanol obtained by using partially *p*-polarized light.

The sensor system was calibrated by using these measurements of three test samples. It is found that the first and the last pixels of the light detector correspond to the angles 33.8057° and 56.8022° with the angular resolution of 0.0029°, respectively. In comparison with the designed values, the angle differences may be caused by a slight misalignment of the distance *AE*. Figure 13 shows the pixel positions on the CMOS sensor that detected the SPRs of air, water and ethanol samples. They fit very well with a black diagonal line, which represents the regression line given by $y = 19221.1243x - 18510.7542$ having a correlation coefficient of 0.9999. The pixel sensitivity of the SPR sensor calculated from the regression line is 5.2026×10^{-5} RIU/pixel. This experimental sensitivity is close to a theoretical value of 5.1627×10^{-5} RIU/pixel for given parameters of the

same sensor. The result is consistent with the resolution of the angular interrogation technique [21].

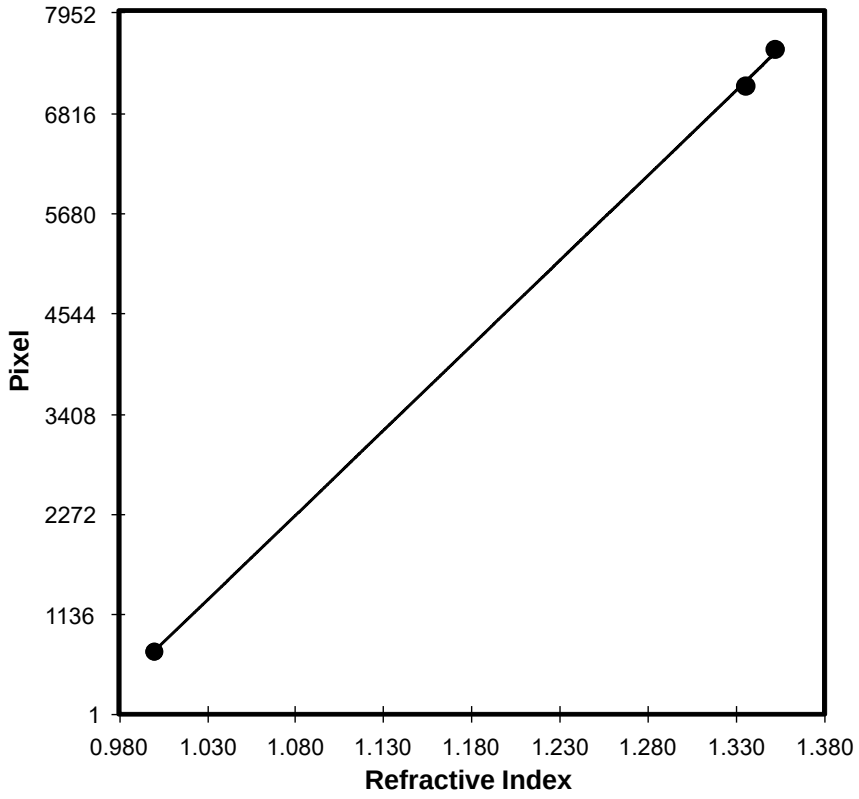

Figure 13. Detected SPR positions as a function of the refractive index of the test samples.

Table 5 presents errors in measurements of the refractive indices and their corresponding resonance angles of the three samples. It is apparent that the refractive index of air can be detected with the smallest error, because it has the sharpest SPR dip. When the width of the SPR dip becomes broader due to the higher refractive index of sample, the error in measurement increases. It is worth mentioning that although the range of the refractive index measurement is broad, the highest error is smaller than 1%. Unlike other SPR sensor, which employs an advanced mathematical transformation to extract the dip SPR [22], our experimental results were obtained by a simple arithmetic averaging. This verifies that the divergent beam produced by the Powell

lens carries uniform energy, yielding the SPR curve with high signal-to-noise ratio. Therefore, this SPR sensor can be used to measure refractive index of sample, which is spatially distributed across the sensing area. The first straight forward application is an implementation of multichannel SPR sensing, where the sensing area is partitioned into multiple sensing elements [23]. Each sensing element detects different analyte. The second application is a large dynamic range SPR. In this application, the SPR can be implemented without the use of high prism refractive index [24]. In summary, the measurement results verify the validity of the beam illumination and detection parameters developed in the preceding section.

Table 5. Errors in measurements of the refractive indices and their corresponding resonance angles of the three samples.

Samples	**Theory**		**Experiment**						
	Pixel	RI	β_{spr}	Pixel	% Error	RI	% Error	β_{spr}	% Error
Air	717	1.0003 [26]	35.878	713	-0.5579	1.0000	-0.02827	35.865	-0.03573
Water	7002	1.3317 [17]	54.104	7107	1.4996	1.3353	0.27097	54.358	0.46921
Ethanol	7675	1.3580 [18]	56.002	7523	-1.9805	1.3520	-0.43908	55.561	-0.78720

Next, sensitivity of the SPR sensor designed to monitor the RI range from 1.3289 – 1.3686 corresponding to the resonance angles from 53.9128° to 56.8022° is considered. Since the sensing area is small, the reflected SPR pattern can be detected by using a smaller light detector such as a commercially available 1/3.6-inch type detector with 1000 × 750 pixels. Theoretical value of this sensor sensitivity can be obtained from the correlation between the detected SPR position and the refractive index shown in Fig. 14 that is 3.973073×10^{-5} RIU. This value is lower than that of the bigger sensing area. Note that this sensitivity is better than fiber-based sensor implemented by

using mobile phone [25]. This reveals that the smaller the sensing area, the better the sensor sensitivity.

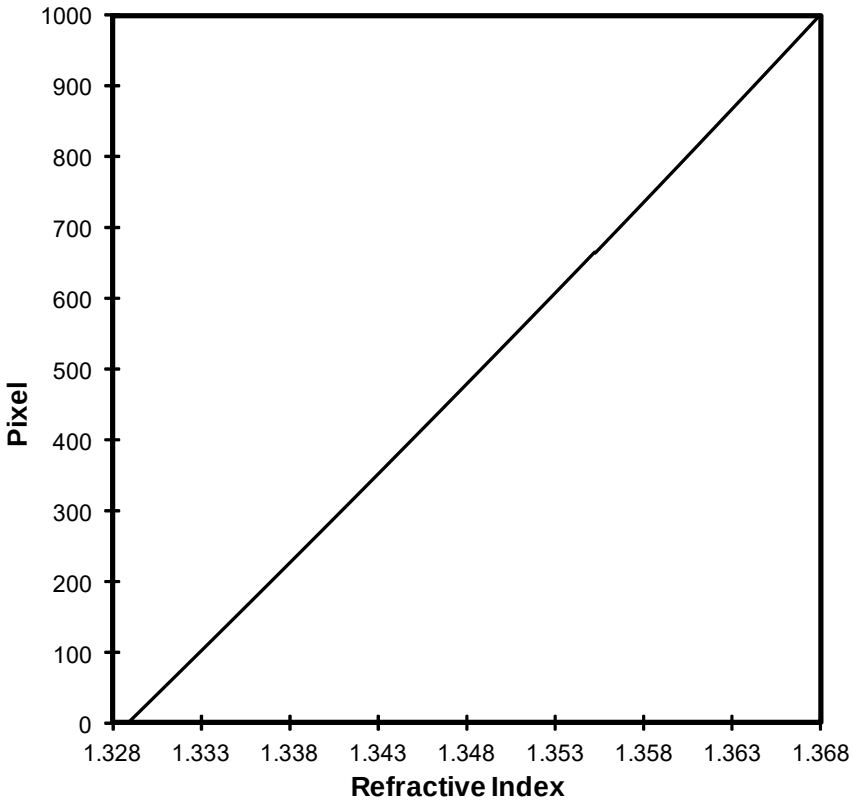

Figure 14. Correlation between the detected SPR position and the refractive index.

5.2 Conclusions

The validity of the optimal divergent beam illumination and detection investigated theoretically in the preceding section has been experimentally verified by using air, water and absolute ethanol as test samples. The experiments were conducted in accordance with the theory of beam parameters. In each experiment, two RIs of samples, air – water and air – ethanol, were simultaneously measured. The errors in the RI measurements are smaller than 1 %, with the sensing of air gives the smallest error, while ethanol is the highest. The increase in error stems from the lower accuracy

in depth detection of the broadened SPR dip. All resultant SPR dips have almost the same lowest depth, regardless of their corresponding resonance angles. Therefore, the results verify that the photon energy carried by the divergent beam can be efficiently transferred to the surface plasmons across a broad sensing area. Finally, it is found that the sensitivity of the SPR using divergent beam is almost the same than other angular interrogation-based SPR. The sensitivity can be improved by reducing the range of RI measurement.

6. Optical Platform of the Handheld SPR Sensor

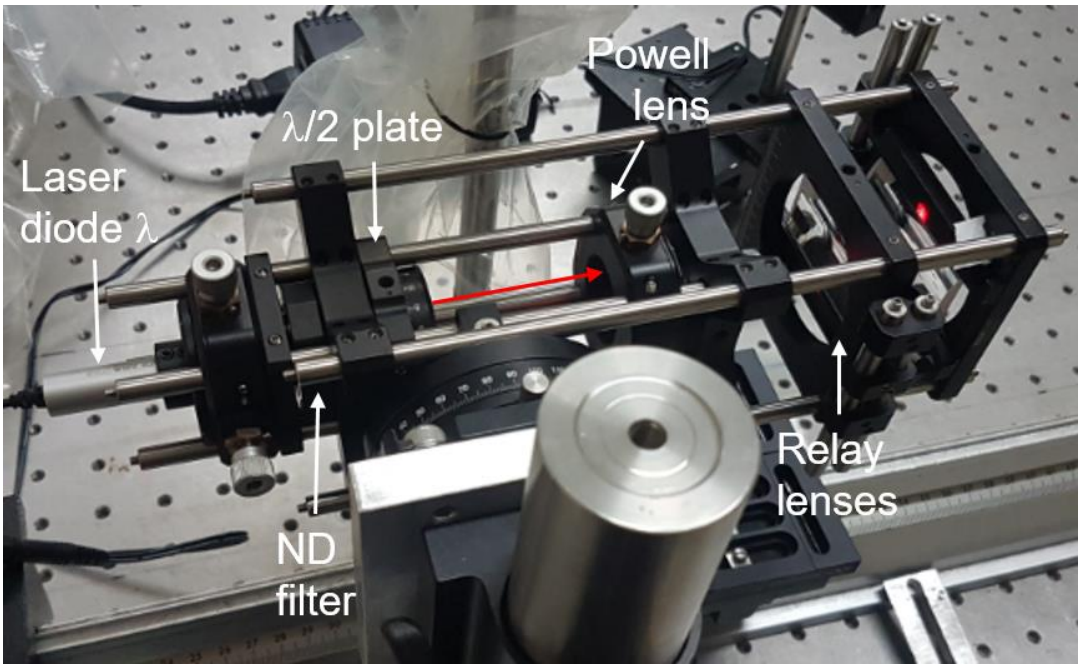

Figure 15. Compact optical platform of the handheld SPR device.

Figure 15 shows compact optical platform of the handheld SPR device constructed by using our proposed architecture. Instead of the HeNe laser, a collimated laser diode with the wavelength λ = 635 nm was used as light source. The half-wave plate maintained its polarization in the *p*-state, while Powell lens provided the divergent beam with uniform energy distribution for multichannel

sensors. The MPTC was fabricated from F2 glass (n_p = 1.620) by using the glass drawing technique. To be able to generate the evanescence wave in the MPTC, a relay lenses focused the beam before the MPTC hypotenuse. As a result the divergent beam incident on the hypotenuse has a small diameter.

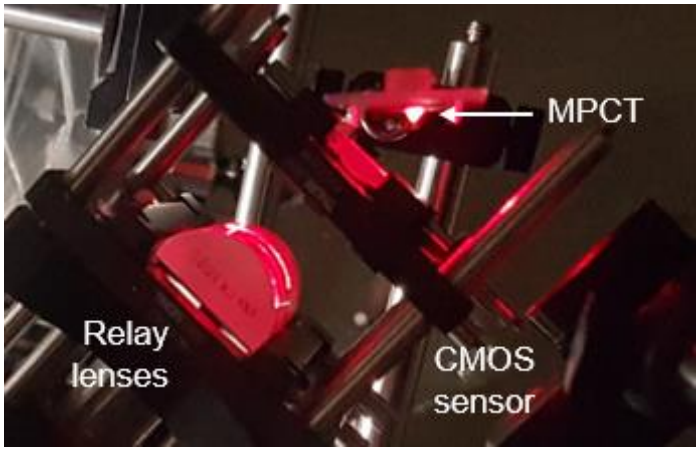

Figure 16. Experimental demonstration of the SPR sensing using the MPTC.

Figure 16 shows the MPTC that was attached to a holder and illuminated by the optical setup described in Fig. 16 at the inclination angle ξ with respect to the horizontal axis. The reflected beam from the MPTC was captured by the same CMOS sensor used in the preceding section. As a proof of concept, the SPR detection of air was experimentally demonstrated.

6.1 Results and Discussions

Figure 17 shows the 1D normalized reflectance of the SPR of air generated by the same arithmetic averaging of the reflectance pattern. Although the SPR dip can be clearly identified, its lowest depth is higher than those of the conventional prism. The energy transfer has the best efficiency of only about 48 %, which is lower than those of the bulky SPR system. This may be mainly caused by the direct coating of the thin gold layer onto the prism did not have good contact, yielding

higher light loss. The illuminating beam was not accurately focused before the sensing area due to the dimension of the MPTC. Currently, these aspects are being studied, while the sensor calibration will be done after the efficiency can be improved.

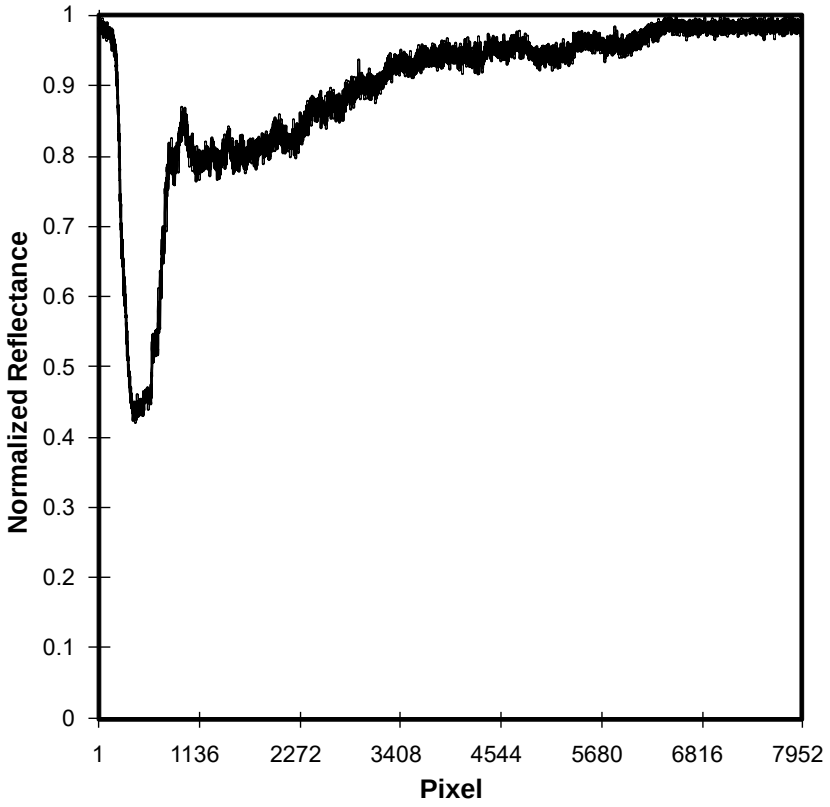

Figure 17. Normalized SPR reflectivity of air obtained by using the handheld SPR sensor.

6.2 Conclusions

The optical platform of the handheld SPR device has been constructed by using the MPTC and tested by sensing air. The experimental result shows that the energy transfer has low efficiency. Besides stringent alignment of the MPTC with respect to the illumination and the detection parts, the low efficiency may be caused by poor quality of the gold layer coated on the micro prism. It is

expected that better quality of the gold coating and use of bigger MPTC may improve the efficiency of this SPR system.

7. Publications

1. J.H. Hossea and J. Widjaja, Design of surface plasmon resonance biosensors by using Powell lens, Proc. iEECON (Int. Electrical Engineering Congress) (2017).
2. J. Widjaja and J.H. Hossea, “Analysis of divergent beam illumination and detection in surface plasmon resonance sensors,” (2018) under submission.

8. References

[1]. A. Otto, Excitation of nonradiative surface plasma waves in silver by the method of frustrated total reflection, Z. Phys. 216, 398-410 (1968).

[2] H. Raether, Surface Plasmons, Berlin, Springler-Verlag, 1988

[3] S.A. Maier, Plasmonics: Fundamentals and Applications, New York, Springer; 2007.

[4] E. Kretschmann and H. Reather, Radiative decay of non radiative surface plasmons excited by light, Z. Naturforsch. A 23, 2135-2136 (1968).

[5] E. Kretschmann, The determination of the optical constants of metals by the excitation of surface plasmons. Z. Phys.241, 313-324 (1971).

[6] R.B.M. Schasfoort and A.J. Tudos, Handbook of Surface Plasmon Resonance, Cambridge: The Royal Society of Chemistry; 2008.

[7] J. Homola, Surface Plasmon Resonance Based Sensors, Springer, New York, 2006.

[8] H.R. Gwon and S.H. Lee, "Spectral and Angular Responses of Surface Plasmon Resonance Based on the Kretschmann Prism Configuration," Mater. Trans. 51, 1150-1155 (2010).

[9] J. Hu, B. Cao, S. Wang, J. Li, W. Wei and Y. Zhao, "Design and fabrication of an angle-scanning based platform for the construction of surface plasmon resonance biosensor," Opt. Lasers Eng. 78, 1-7 (2016).

[10] N. Tao, S. Boussaad and W. Huang, "High resolution surface plasmon resonance spectroscopy," Rev. Sci. Instrum. 70, 4656-4660 (1999).

[11] T.M. Chinowsky, J.G. Quinn, D.U. Bartholomew, R. Kaiser and J.L. Elkind, "Performance of the Spreeta 2000 integrated surface plasmon resonance affinity sensor," Sens. Actuators B Chem. 91, 266-274 (2003).

[12] B.L. Chan BL and S. Jutamulia, “SPR prism sensor using laser line generator,” Proc. SPIE 8234, 82341P (2012).

[13] S. Isaacs and I. Abdulhalim, “Long range surface plasmon resonance with ultra-high penetration depth for self-referenced sensing and ultra-low detection limit using diverging beam approach,” Appl. Phys. Lett. 106, 193701 (2015).

[14] R. Chen, M. Wang, S. Wang, H. Liang, X. Hu, X. Sun, J. Zhua, L. Ma, M. Jiang, J. Hua and J. Li, A low cost surface plasmon resonance biosensor using a laser line generator, Opt. Commun. 349, 83-88 (2015).

[15] K. Chang, R. Chen, S. Wang, J. Li, X. Hu, H. Liang, B. Cao, X. Sun, L. Ma, J. Zhu, M. Jiang and J. Hu, Considerations on circuit design and data acquisition of a portable surface plasmon resonance biosensing system, Sensors 15, 20511-20523 (2015).

[16] B.L. Chan and S. Jutamulia, Micro-prism test chip, US Patent US 2015030.0954A1 22 Oct. 2015.

[17] G. M. Hale and M. R. Querry. Optical constants of water in the 200-nm to 200-μm wavelength region, Appl. Opt. 12, 555-563 (1973).

[18] C. Fan and J.P. Longtin, Laser-based measurement of temperature or concentration at a solid-liquid interfaces, Exp. Therm. Fluid Sci. 23, 1-9 (2000).

[19] M. Yamamoto, “Surface plasmon resonance (SPR) theory: Tutorial,” Rev. Polarogr. 48, 209-237 (2002).

[20] J.P. Longtin and C. Fan, “Precision laser-based concentration and refractive index measurement of liquids,” Micros. Therm. Eng. 2, 261-272 (1998).

[21] J. Homola, S.S. Yee and G. Gauglitz, “Surface plasmon resonance sensors: review,” Sens. Actuators B Chem. 54, 3-15 (1999).

[22] A. Karabchevsky, S. Karabchevsky and I. Abdulhalim, “Fast surface plasmon resonance imaging sensor using Radon transform,” Sens. Actuators B Chem. 155, 361-365 (2011).

[23] M. Vala, K. Chadt, M. Piliarik, J. Homola, “High-performance compact SPR sensor for multi-analyte sensing”, Sens. Actuators B Chem. 148, 544-549 (2010).

[24] J. Canning, J. Qian and K. Cook, “Large Dynamic Range SPR Measurements Using a ZnSe Prism,” Photonic Sens. 5, 273-283 (2015).

[25] K. Bremer and B. Roth, “Fibre optic surface plasmon resonance sensor system designed for smartphones,” Opt. Express 23, 17179-17184 (2015).

[26] J. Workman, The Handbook of Organic Compounds, San Diego, Academic Press, 2001.